An X_0 shim coil for precise magic-angle adjustment

Tatsuya Matsunaga [a], Takashi Mizuno [b], K. Takegoshi [a,*]

[a] *Division of Chemistry, Graduate School of Science, Kyoto University, 606-8502 Kyoto, Japan*

[b] *JEOL RESONANCE Inc., 196-8558 Akishima, Tokyo, Japan*

Abstract

A new method for precise setting of the spinning angle to the magic angle by using a saddle coil is described. The coil, which is referred to as an X_0 shim coil, is wound to produce a uniform static magnetic field B_x perpendicular to the main magnetic field B_0. The magnetic field felt by a sample is a vector sum of the main field B_0 and the transverse field B_x produced by the X_0 shim coil. Hence the angle between the spinner axis and the effective magnetic field can be controlled by current I supplied to the X_0 shim coil, leading to precise angle adjustment without backlash accompanied with a mechanical system conventionally used. It is shown that the angle range achieved is $\pm 0.05^\circ$ for $I = \pm 5$ A at $B_0 = 7$ T.

Key words: X_0 shim coil, MAS, high resolution solid state NMR

* corresponding author; takeyan@kuchem.kyoto-u.ac.jp

1 Introduction

In high-resolution solid-state NMR, magic angle spinning (MAS)[1] is an indispensable technique to remove anisotropic interactions. Under MAS, the anisotropic spin interactions such as the dipolar and chemical shielding interactions are modulated by sample spinning, and their secular parts are scaled by $\frac{1}{2}(3\cos^2\theta - 1)$, where θ is the angle between the spinner axis and the external main magnetic field B_0. By setting θ to the "magic angle" $\theta_{\mathrm{MA}} = \arccos\frac{1}{\sqrt{3}} \approx 54.74°$, one can remove the secular part of an anisotropic interaction. Hereafter, we refer θ to as the spinning angle.

Conventionally, the spinning angle θ is adjusted by a mechanical gear system, and, with the backlash of a gear, precise adjustment is difficult. Small deviation from the exact magic angle may be appreciable in some experiments. A remarkable case is ST-MAS for half-integer quadrupolar nuclei. It was shown that the angle deviation over 0.008° would bring appreciable broadening to the ^{23}Na ST-MAS line shape of Na_2SO_4, whose quadrupoler coupling constant is 2.560 MHz[2]. Fine setting of the spinning angle by a mechanical way is also a troublesome process to observe a 1D spectrum of a nuclear which has a large anisotropic interaction, for example, ^{2}H with a large quadrupole interaction[3] and ^{195}Pt with a large chemical shift anisotropy[4]. Hence the precise setting of the spinning angle by a non-mechanical way should be secured in many situations of solid state NMR.

In this work, we develop a new method for precise setting of the spinning angle, that is, tilting the static magnetic field felt by a sample by applying an additional static field perpendicular to the main magnetic field B_0. Throughout this work, we define the z axis parallel to B_0, and the x-axial additional field vertical to B_0 is hence written as B_x. It's produced by a saddle coil attached to a MAS probe, which we shall refer to as an X_0 shim coil[5].

In this work, we estimate spacial inhomogeneity of B_x and also an additional "redundant" magnetic field along the z axis (B_z) produced by the X_0 shim coil. The geometry and the size of the X_0 shim coil are then determined to keep line broadening caused by B_x and B_z less than 0.05 ppm at $B_0 = 7$ T. As for the range of adjustable angle achieved by the X_0 shim coil, we thought ca. $\pm 0.05^\circ$ would be enough, as we are going to use the classical gear system for coarse adjustment in conjunction with the X_0 shim coil. With the coil dimensions given in this work, we show that the current for the X_0 shim coil to achieve the range of $\pm 0.05^\circ$ for $B_0 = 7$ T becomes ± 5 A. Application of ± 5 A is feasible, however, the current would bring some practical problems due to Joule heat and Lorentz force. We show that temperature rising due to the Joule heat can be suppressed by air cooling and further by turning off the current during the relaxation delay of a NMR pulse sequence. For the Lorentz force, we show that the tilting of the X_0 shim coil by the Lorentz force can be reduced largely by fabricating the X_0 shim coil on a firmly built and fixed mounting retainer, which is used as a cap for a MAS probe. We further

show that accumulation of residual slight tilting of the X_0 shim coil during repeated signal acquisition can be avoided by applying opposite current after each signal acquisition.

2 The X_0 shim coil

In section 2.1, the configuration of the X_0 shim coil is illustrated to define the effective field and its tilt angle from the static field. In section 2.2, for an ideal one-turn X_0 shim coil, we derive equations for the magnetic field produced at a general point. In section 2.3, its optimum geometry is determined by examining the magnetic fields at the position of the sample. In section 2.4, a 50-turn X_0 shim coil actually used is examined, and in section 2.5, the performance of the X_0 shim coil is discussed. Finally in section 2.6, we examine the practical problems due to the Joule heat and the Lorentz force.

2.1 The configuration of the X_0 shim coil

Fig. 1a illustrates the configuration of the X_0 shim coil. In the figure, $2a, 2l$, and 2α designate the diameter, the height, and the gap angle between two opposite arcs, respectively. The angle between the spinner axis in the xz plane and the static field along the z axis is written as θ. In Fig. 1b, we define two angles, ε and $\Delta\theta$. The angle ε in the xz plane represents misalignment of the X_0 shim coil from the x axis, which may be written as

$$\varepsilon = \varepsilon_0 + \varepsilon(I), \tag{1}$$

where ε_0 denotes the static misalignment, and $\varepsilon(I)$ represents tilting of the coil axis by the Lorentz force. We shall refer ε to as the coil-tilt angle. The tilt angle $\Delta\theta$ of the effective field B_{eff} is written as

$$\Delta\theta = \frac{180}{\pi}\arctan[\frac{B_{\text{eff}}^2 + B_x^2 - B_0^2}{2B_0 B_{\text{eff}}}] \approx \frac{180}{\pi}\frac{B_x}{B_0}\ [\text{degree}], \tag{2}$$

where B_{eff} is the size of the effective field given by

$$B_{\text{eff}} = \sqrt{B_0^2 + B_x^2 - 2B_0 B_x \sin\varepsilon} \approx B_0 + \frac{B_x^2}{2B_0} - \frac{\pi}{180}B_x\varepsilon. \tag{3}$$

Note here that B_{eff} causes a signal shift δ written as

$$\delta = \frac{B_{\text{eff}} - B_0}{B_0} \approx \frac{B_x^2}{2B_0^2} - \frac{\pi}{180}\frac{B_x}{B_0}\varepsilon, \tag{4}$$

and the spinning angle becomes $\theta - \Delta\theta$.

2.2 Magnetic fields produced by the X_0 shim coil

In this section, we evaluate the magnetic field produced by the X_0 shim coil. A saddle coil with an infinite height ($2l = \infty$) does not produce magnetic field along z. For a coil with a finite height, however, the z-magnetic field is zero only at the coil center designated as $\boldsymbol{O}$ in Fig. 1, and the z-magnetic field at a general position $\boldsymbol{P}$ ($B_z(\boldsymbol{P})$) would result in line broadening. In other words, the height of the X_0 shim coil should be optimized to reduce spacial variation of $B_z(\boldsymbol{P})$ over the sample.

The y-magnetic field produced by the X_0 shim coil is small at the sample position, and, moreover, its effect on the linewidth would be averaged out by the sample spinning. Therefore, we ignore the y-magnetic field in this work.

The x-magnetic field B_x is the main field produced by the X_0 shim coil. As shown below, B_x is spacially distributed, and the distributed $B_{\rm eff}$ and $\Delta\theta$ cause line broadening. As broadening due to spacial variation of $\Delta\theta$ would be quite small, it is ignored in this work. We thus examine only line broadening due to spacially distributed $B_{\rm eff}$ through Eq. (4). The task is therefore to obtain a coil geometry, which maximizes $B_x(\boldsymbol{O})$ without increasing $\Delta B_x(\boldsymbol{P}) \equiv B_x(\boldsymbol{P}) - B_x(\boldsymbol{O})$ and $B_z(\boldsymbol{P})$ appreciably.

The magnetic field produced by the X_0 shim coil is calculated separately for the arc parts and for the vertical-line parts. We shall refer the magnetic fields produced by the former and the latter to as $\boldsymbol{B^A}$ and $\boldsymbol{B^L}$, respectively. As discussed above, the y-components of $\boldsymbol{B^A}$ and $\boldsymbol{B^L}$ are ignored. The z-magnetic field produced from the line parts (B_z^L) can be negligible when the lines are almost parallel to the z axis. Thus, we evaluate B_x^A, B_x^L, and B_z^A in the following. For simplicity, we assume one-turn coil with infinitely thin wire.

For the arc parts, the differential magnetic field $d\boldsymbol{B^A}$ at $\boldsymbol{P}$ produced by current at a point $\boldsymbol{Q}$ in the arc is described by the Biot-Savart law written as

$$d\boldsymbol{B^A} = \frac{\mu_0 I}{4\pi} \int_C \frac{d\boldsymbol{s} \times \overrightarrow{QP}}{|QP|^3}. \tag{5}$$

Here, $d\boldsymbol{s}$ represents the line element on $\boldsymbol{Q}$ of the X_0 shim coil. The z- and x-

elements of $\boldsymbol{B_A}$ are given by

$$B_z^A(\boldsymbol{P}) = \frac{\mu_0}{4\pi}\int_{C_{\rm up}} \frac{aR\cos(\phi'-\phi)-a^2}{[a^2+R^2+(z-l)^2-2aR\cos(\phi'-\phi)]^{3/2}}d\phi' + \frac{\mu_0 I}{4\pi}\int_{C_{\rm low}} \frac{aR\cos(\phi'-\phi)-a^2}{[a^2+R^2+(z+l)^2-2aR\cos(\phi'-\phi)]^{3/2}}d\phi', \quad (6)$$

and

$$B_x^A(\boldsymbol{P}) = \frac{\mu_0 I}{4\pi}\int_{C_{\rm up}} \frac{-a(z-l)\cos\phi'}{[a^2+R^2+(z-l)^2-2alR\cos(\phi'-\phi)]^{3/2}}d\phi' + \frac{\mu_0 I}{4\pi}\int_{C_{\rm low}} \frac{-a(z+l)\cos\phi'}{[a^2+R^2+(z+l)^2-2alR\cos(\phi'-\phi)]^{3/2}}d\phi', \quad (7)$$

respectively. Here, (R, ϕ, z) and (a, ϕ', l) are the polar coordinates of $\boldsymbol{P}$ and $\boldsymbol{Q}$, and $C_{\rm up}$ and $C_{\rm low}$ represent integral paths for the upper- and lower-arc pairs, respectively, whose explicit forms are explicitly given in the supplementary materials (Fig. S1 and Eq. S1).

For the line part, the differential magnetic field $d\boldsymbol{B^L}$ at $\boldsymbol{P}$ is described as

$$d\boldsymbol{B^L} = \frac{\mu_0 I}{4\pi}\frac{adz\sin\xi}{|QP|^2}, \quad (8)$$

where ξ is the angle between current I on $\boldsymbol{Q}$ and $\overrightarrow{QP}$. As have discussed above, we ignore B_z^L and B_y^L, and the integration of B_x^L can be done analytically for each line part. The explicit integral paths and the corresponding B_x^L are given in the supplementary materials (Fig. S2 and Eq. S2).

2.3 Optimization of the height of the X_0 shim coil

At the center of the coil $\boldsymbol{O}$, Eqs. (7) and (8) (and Eq. (S2-5) in supplementary materials) lead the following x-magnetic fields,

$$B_x^A(\boldsymbol{O}) = \frac{2\mu_0 I}{\pi} \frac{al\cos\alpha}{(a^2+l^2)^{3/2}} \tag{9}$$

and

$$B_x^L(\boldsymbol{O}) = \frac{2\mu_0 I}{\pi} \frac{l\cos\alpha}{a\sqrt{a^2+l^2}}, \tag{10}$$

respectively. The total x-magnetic field produced by the X_0 shim coil $B_x(\boldsymbol{O}) = B_x^A(\boldsymbol{O}) + B_x^L(\boldsymbol{O})$ becomes

$$B_x(\boldsymbol{O}) = \frac{2\mu_0 I}{\pi} \frac{(2a^2+l^2)l\cos\alpha}{a(a^2+l^2)^{3/2}}. \tag{11}$$

Eq. (11) implies that the strongest $B_x(\boldsymbol{O})$ is achieved with the height $2l$ being equal to $2\sqrt{2}a$ and the coil diameter $2a$ and the gap angle 2α being as small as possible. Practically, the gap angle α can not be zero, and we assume $\alpha \sim 15°$ for our X_0 shim coil. The α value does not affect magnetic homogeneity around the sample appreciably as compared to the other two parameter ($2a$ and $2l$), and α-dependent inhomogeneity is ignored. The coil diameter $2a$ is set to 66.4 mm as we are to wind the X_0 shim coil around the MAS probe whose diameter is ca. 66 mm. The optimal coil height for the maximum $B_x(\boldsymbol{O})$ is therefore $l = \sqrt{2}a \sim 47$ mm. However, in the following, we show that the unwanted z-field $B_z(\boldsymbol{P})$ is also large at $l = \sqrt{2}a$.

To appreciate the spacial distribution of B_x and B_z along the axis of

the sample, we introduce a new coordinate d to designate position in the sample (Fig. 2a). The center $\boldsymbol{O}$ is denoted by $d = 0$ mm, and the both ends of the sample, since the sample length of the 5 mm rotor we use is ca. 4.5 mm, correspond to $d = \pm 2.3$ mm. We shall refer to $d = 0$ mm and $d = 2.3$ mm as d_0 and d_{end}, respectively, and use $B_z(d_{\mathrm{end}})$ as a measure of the spacial inhomogeneity of $B_z(\boldsymbol{P})$. $B_x(d_0)$ and $B_z(d_{\mathrm{end}})$ are calculated for various coil heights $2l$ with $I = 1$ A using Eqs. (11) and (6), and the results are shown in Figs. 2b and 2c, respectively. As indicated by Eq. (11), $B_x(d_0)$ becomes maximum at $l = \sqrt{2}a \sim 47$ mm. However, at $l = 47$ mm, the redundant magnetic field $B_z(d_{\mathrm{end}})$ becomes ca. -9.5 nT, which corresponds to 1×10^{-3} ppm at 7 T. In Fig. 2c, it is notable that at $l \simeq 2a \sim 66.4$, $B_z(d_{\mathrm{end}})$ become ca. 0 T. We therefore chose $l \simeq 2a \sim 66.4$ mm as a compromised height for large $B_x(d_0)$ and small $B_z(d_{\mathrm{end}})$.

2.4 The geometry of the X_0 shim coil

So far, we considered an ideal coil (an one-turn X_0 shim coil with infinitely thin wire) for ease of calculation. In practice, the larger turn number is better as it produces larger B_x. For the X_0 shim coil, wire with a round section (round wire) is not suitable as there are large Arbelos-shaped gaps among the adjacent turns of the wire (Fig. 3a), which causes low electric-conductivity per turn and poor effluence of the Joule heat. In addition, it is mechanically fragile against the Lorentz force because of pliability of round wire in any direction. Thus, we wound the X_0 shim coil by using wire with a

rectangular section (rectangular wire) with the longer side of the wire section standing perpendicularly to the coil surface ('flatwise' winding). It has smaller gaps among the adjacent turns of the wire than that wound with the round wire (Fig. 3b). The larger contact areas between the adjacent turns and also that between the wire and the coil bobbin improve the effluence of the Joule heat. Furthermore, it is robust against the plastic deformation by the Lorentz force.

An illustration of one of the pair of the flatwise-wound saddle coil is shown with a part of its outmost turn in Fig. 3c. The width and the thickness of the wire are 2.6 mm and 0.3 mm, respectively. We wound a 50-turn coil, and the interval between the adjacent turns of wire is 0.34 mm, hence the actual size parameters of the X_0 shim coil, the diameter, the length and the gap angle, becomes $2a$ =66.3–71.5 mm, $2l$ = 123.6–157.2 mm and 2α =10–70°, respectively.

To maintain the coil against the Lorentz force, the X_0 shim coil is wound in grooves cut on the surface of a duralumin body of a mounting retainer. The pictures of the X_0 shim coil on the retainer and the MAS probe are given in the supplementary materials (Fig. S3). Fig. 4 shows a cross-section sketch of an X_0 shim coil and a MAS probe in a magnet with a room-shim unit. The X_0 shim coil is used as the "shielding cap" of the MAS probe, which is fixed by the bolts with the room-shim unit. The retainer with the X_0 shim coil is fixed at the top of the main magnet and by the O-ring to the main magnet

at the flank. Further, the bottom of the flank has a cut to couple closely with the top of the room-shim unit.

In the following calculation, the actual width of the wire is taken into account approximately by expressing the wire as a bundle of 10 separated wires with a width of 0.26 mm. In other words, we assume that the magnetic field produced by 1 A current flowing through one flat wire with its width of 2.6 mm can be calculated as a sum of 10 magnetic fields produced by 0.1 A current flowing through 10 thin wires aligned with the interval of 0.26 mm perpendicularly to the coil surface.

2.5 The calculated performance of the X_0 shim coil

The magnetic fields $B_x^A(\boldsymbol{O})$ and $B_x^L(\boldsymbol{O})$ obtained by integrating Eqs. (9–11) for the 50-turn coil with $2l$ =123.6–157.2 mm and 2α =10–70° become

$$B_x^A(\boldsymbol{O}) \simeq 1.89 \times 10^{-4} I \text{ [T]} \tag{12}$$

and

$$B_x^L(\boldsymbol{O}) \simeq 9.59 \times 10^{-4} I \text{ [T]}, \tag{13}$$

respectively, and the total x magnetic field is

$$B_x(\boldsymbol{O}) = B_x^A(\boldsymbol{O}) + B_x^L(\boldsymbol{O}) \simeq 1.15 \times 10^{-3} I \text{ [T]}. \tag{14}$$

For $B_0 = 7$ T, Eq. (14) leads the angle $\Delta\theta$ (Eq. (2) and Fig. 1) written as

$$\Delta\theta \simeq 9.33 \times 10^{-3} I \text{ [degree]}, \tag{15}$$

and the additional shift δ (Eq. (4)) is given by

$$\delta \simeq 1.32 \times 10^{-2} I^2 - 2.84(\varepsilon_0 + \varepsilon(I))I \text{ [ppm]}. \tag{16}$$

Eq. (15) shows that we can adjust the angle within $\pm 0.05^\circ$ for $I = \pm 5$ A.

Here, we examine the redundant magnetic fields $B_x(d)$ and $B_z(d)$. The calculated $B_x(d)$ for $I = 1$ A (Fig. 5a) shows that the difference $\Delta B_x \equiv B_x(d_0) - B_x(d_{\text{end}})$ is ca. 1.5 μT for $I = 1$ A. Hence it would be ca. 7.5 μT for $I = 5$ A. Line broadening Δ_x due to the variation of the x-field ΔB_x can be estimated by using Eq (4) as

$$\Delta_x \approx \left(\frac{B_x(d_0)}{B_0^2} - \frac{\pi}{180} \frac{\varepsilon}{B_0} \right) \Delta B_x. \tag{17}$$

For $\varepsilon = 0$, ΔB_x for $I = 5$ A corresponds to line broadening of 9×10^{-4} ppm at 7 T. In the following, we show that the experimentally obtained ε is about -0.1° to -0.2°. Hence line broadening due to ΔB_x is less than 0.005 ppm at 7 T, and broadening due to ΔB_x is negligible.

Fig. 5b shows the calculated $B_z(d)$ for $I = 1$ A. As the z component acts directly to the resonance frequency, its distribution is of most concern. The estimated variation of $B_z(d)$ over $\pm d_{\text{end}}$ is 0.12 nT, which corresponds to 2×10^{-5} ppm line broadening at 7 T. Hence, this can also be ignored. Practically, however, these broadening effects may become appreciable due to deformation of the coil shape from the ideal one and displacement between the sample and the coil center. Hence, we examine a way to reduce line broadening

in advance.

It is notable that both $B_x(d)$ and $B_z(d)$ can roughly be expressed by a function of d^2 for the range of $[-d_{\mathrm{end}}, d_{\mathrm{end}}]$. In the Cartesian coordinate (x, y, z), d^2 can be written by

$$d^2 = z^2 + x^2 = \frac{3\sqrt{2}}{2}xz. \tag{18}$$

Thus, line broadening due to the inhomogeneous magnetic field produced by the X_0 shim coil can be reduced by adjusting the xz term of the room-shim coil (C_{xz}). Therefore, we firstly obtain optimal C_{xz} values for several I values by observing the ^{1}H MAS NMR signal of H_2O. The observed C_{xz} values are least-square fitted to $C_{xz} = aI^2 + bI + c$, with a, b, and c as adjustable parameters (Fig. S4 in the supplementary materials) and used for further experiments. To conclude, the line broadening caused by the redundant magnetic field may be appreciable but can be removed by the C_{xz} correction.

2.6 Joule heat and Lorentz force

Since the resistance of the X_0 shim coil is ca. 1.2 Ω, $I = 5$ A produces 30 W Joule heat. In fact, we found that the Joule heat increases the temperature of the X_0 shim coil by 11 °C. However, the Joule heat problem can be overcome mostly by flowing cooling air from the bottom of the probe with the rate of 70 L/min, which reduces the temperature increment of the X_0 shim coil from 11°C to 4°C for $I = 5$ A. Further reduction was made by turning off the X_0-shim current during the relaxation delay. An example of the on/off timing

sequence is given for a single-pulse experiment as shown in Fig. 6. The explicit temperature data of the X_0 shim coil and the probe are shown in Fig. S5 of the supplementary materials.

For the given coil dimensions, we estimated the Lorentz force to be 220 N at the top and bottom of the coil, which acts to bring the "x-axis" of the X_0 shim coil parallel to the main magnetic field B_0. As described above, the X_0-shim-coil body (the retainer) has a role to sustain the X_0 shim coil against the Lorentz force (Fig.4). Even with the retainer, we found that a small deviation of the angle caused by the Lorentz force is accumulated during repeated signal acquisition. To avoid such accumulation, we put opposite current after each signal acquisition. A schematical timing chart is given in Fig. 6. We shall refer this procedure to as the $-I$ procedure in the following. The effect of the opposite current is described in section 4.

3 Experimental

NMR measurements were done for $B_0 = 7.05$ T (JASTEC Co. Ltd.) using an OPENCORE[6] spectrometer operating at the resonance frequencies of 301.4 MHz for ^{1}H, 75.8 MHz for ^{13}C, and 42.3 MHz for ^{2}H with a MAS probe (Doty Scientific, Inc.) for a 5 mm rotor. We measured ^{1}H MAS NMR of H_2O doped with 5 mM $CuSO_4$, ^{13}C CPMAS NMR of adamantane, and ^{2}H MAS NMR of partially deuterated dimedone-2,3-d_2. In ^{1}H MAS NMR, 5 mM $CuSO_4$ aqueous solution was packed in a homemade sealed cell. Adamantane was purchased from Wako Pure Chem. Ind. Ltd. Dimedone was purchased

from Tokyo Chem. Ind. Ltd., and the dimedone-2,3-d_2 sample for ^{2}H NMR was obtained by recrystallizing dimedone from 99.9 % ^2H_2O (Sigma-Aldrich Co. Ltd.) solution for 3 times[3]. The ^{13}C CPMAS spectra of adamantane were obtained under ^{1}H CW decoupling, while the ^{2}H MAS spectra was obtained without decoupling. For all experiments, 5 dummy scans were applied before starting each accumulation, and the $-I$ procedure (Fig. 6) was used unless otherwise denoted. The spinning frequency was ca. 500 Hz for ^{1}H and 10 kHz for ^{13}C and ^{2}H, respectively. The current through the X_0 shim coil was controlled by using a bipolar power supply (PBX20-20, KIKUSUI ELECTRONICS Corp.), whose resolution is 1 mA.

4 Results and discussions

In this section, we firstly examine line broadening caused by the X_0 shim coil by observing the ^{1}H spectrum of H_2O, and secondly, the tilting of the X_0 shim coil due to the Lorentz force is examined by monitoring the shift of the ^{13}C peak of CH_2 of adamantane. Then the precise setting of the spinning angle is demonstrated for the ^{2}H MAS spectrum of partially deuterated dimedone.

Fig. 7 shows the I dependence of full width at half maximum (FWHM) of ^{1}H MAS NMR spectra of H_2O of 5 mM $CuSO_4$ aqueous solution spinning at 500 Hz with and without the C_{xz} correction. For experiments with the C_{xz} correction, the linewidth varies only from 0.012 ppm to 0.014 ppm for $I = -5$ A to 5 A, while for those without the C_{xz} correction, it varies from 0.010 to 0.021 ppm. The additional linewidth without the C_{xz} condition is thus 0.011

ppm, which is larger than that calculated (∼0.005 ppm) in section 2.5 . The larger broadening may be caused by displacement between the sample center and the center of the X_0 shim coil and/or deformation of the coil shape from the ideal one. Since the line broadening of 0.011 ppm is small enough for most of solid state NMR experiments, the C_{xz} correction is not a mandatory procedure.

Fig. 8 shows ^{13}C CPMAS NMR spectra of adamantane at various current I for the X_0 shim coil. It is notable that the signal-to-noise ratio deteriorated with varying the current I from 5 A to -5 A, which is ascribed to CP mis-matching due to the peak shift δ[7]. The apparent peak shift δ is ascribed to the size change of the effective field $B_{\rm eff}$ and the tilting of the coil $\varepsilon(I)$ by the Lorentz force (Eqs. (4) and (16)). We obtained $\varepsilon(I)$ from the observed $\delta(I)$ by using Eq. (16) and plotted in Fig. 9. The observed $\varepsilon(I)$ can be least-squares fitted to a straight line, and the result is

$$\varepsilon = \varepsilon_0 + \varepsilon(I) = -0.135 - 0.0082I \text{ [degree]}. \tag{19}$$

This shows that the present X_0 shim coil was built with static misalignment of $\varepsilon_0 = -0.135^\circ$, and the Lorentz force further changes the angle by 0.0082° per 1 A. Practically, as long as the angle stays constant during the NMR experiment, the I dependence of the coil-tilt angle ε is not a serious problem. In adjusting process of the spinning angle, however, hysteresis of ε against current I is cumbersome. We therefore examined hysteresis of ε by changing current I in

three deferent ways; (1) increasing from -5 A to 5 A, (2) starting from 0 A, and increased to 5 A and jumped back to 0 A followed by decreasing to -5 A, and (3) changing rather randomly as $0, 5, -0.5, 4.5 \cdots$ A. The observed $\varepsilon(I)$ for the three experiments (Fig. S6 in the supplementary materials) can also be described by Eq. (19) with the standard deviation of $(1.4 \times 10^{-3})^\circ$. This small hysteresis ensures high reproductivity even in the setting process of the magic angle.

During long signal accumulation, the coil-tilt angle ε may change gradually. To examine the long-time behavior with and without the $-I$ procedure in the pulse sequence, we examined ε for 16 hours at $I = \pm 5$ A. The pulse repetition time and the accumulation number for one measurement were 4.8 sec and 50 times, respectively. With adding 5 dummy scans, the total experimental time for one measurement was 250 sec. The measurement was repeated 240 times, and variation of ε obtained for each measurement is plotted in Fig. 10. For $I = 5$ A with the $-I$ procedure (represented by the open circles), ε increased by $(2.2 \times 10^{-3})^\circ$ in the first one hour and stayed there with the standard deviation of $(3 \times 10^{-4})^\circ$. Similarly, for $I = -5$ A, ε increased by $(2.3 \times 10^{-3})^\circ$ in the first 1 hour and stayed there with a standard deviation of $(2 \times 10^{-4})^\circ$. In both cases, ε changes only a few 10^{-3} degrees, which does not deteriorate spectral resolution in most of the MAS experiments. When angle stability of a few 10^{-4} degrees is required, one should wait for an hour with applying the pulse sequence before starting signal accumulation. Time

variation of ε without the $-I$ procedure is also shown in Fig. 10 (the crosses); ε kept changing even after 16 hours.

Fig. 11 shows the ^{2}H MAS NMR spectra of partially-deuterated dimedone observed at various current I. Due to the quadrupolar interaction of ^{2}H, the spinning sidebands spread over 6600 ppm, and their peak heights are very sensitive to deviation of the spinning angle from the exact magic angle. Before precise adjustment by using the X_0 shim coil, we coarsely adjusted the angle of the spinner axis θ by using a mechanical gear system with monitoring ^{79}Br MAS NMR of KBr[8]. Note that we used different spinners for KBr and dimedone, and the sample changing would caused a slight change in orientation of the stator. Fig. 11 indicates that the spinning angle set by the KBr method ($I = 0$ A) is slightly deviated from the exact magic angle. Also we found that the current range (-5 to 5 A) is wide enough to bring $\theta - \Delta\theta$ to $\theta_{\rm MA}$, which is realized by current $I \sim -1$ A in this case. For precise setting of the spinning angle, we plotted the sum of the peak intensities of the sidebands at various I in Fig. 12, which shows that the best matching to the magic angle is obtained at $I = -0.8$ A. Fig. 12 also shows that the precision/stability required for current is ca. ± 0.01 A, which is well satisfied in the present equipment.

Lastly, we would like to point out that a fully automated "magic-angle stabilizer" may be realized when one combines the X_0 shim coil and a device that detects the spinning angle. As for the latter device, one may use a Hall sensor developed by S. Mamone *et al.*[9] or an optical detection scheme

developed by E. Mihaliuk and T. Gullion[10].

5 Summary

In this work, we presented the X_0 shim coil for precise setting of the spinning angle for MAS NMR. The X_0 shim coil produces an additional static magnetic field B_x perpendicular to the main magnetic field B_0 and tilts the effective magnetic field.

We examined the coil configuration for a larger magnetic field B_x without introducing appreciable magnetic-field inhomogeneity over the sample. We found that the optimal coil geometry is the coil height being about twice of the coil diameter, $l \sim 2a$. Under the practical geometrical restriction such as the bore size of the main magnet and the MAS probe, the turn number of the coil became 50 and its diameter, the length, and the gap angle were decided to be 66.3–71.5 mm, 123.6–157.2 mm, and 10–70°, respectively. With these values, we estimated that the range of the adjustable angle by the X_0 shim coil is $\pm 0.05°$ at $B_0 = 7$ T for $I = \pm 5$ A, and line broadening due to the redundant magnetic fields is less than 0.05 ppm.

To overcome the Joule heat and particularly the Lorentz force problems, we wound the coil using rectangular wire with flatwise winding. In addition to this, cooling air and the turning-off step of current in a pulse sequence helped to reduce temperature increment by the Joule heat only 1°C. To resist the Lorentz force, we fixed the mounting retainer with the X_0 shim coil firmly to

the room-shim unit and the main magnet. Furthermore, we showed that the $-I$ procedure in the pulse sequence reduces accumulation of the tilting of the X_0 shim coil during long signal acquisition.

^{1}H NMR measurement of H_2O showed that the line broadening due to the X_0 shim coil is only 0.011 ppm. It can be reduced further down to 0.002 ppm by the xz-term correction of the room shim. ^{13}C NMR measurement of adamantane showed high stability against the Lorentz force. ^{2}H spectra of demedone-2,3-d_2 showed that the spinning angle can be adjusted straightforwardly to the magic angle.

Acknowledgment

This work was financially supported by Japan Science and Technology Agency (JST). We thank Uratani Engineering, Inc., for winding the X_0 shim coil.

References

[1] E.R. Andrew, A. Bradbury and R.G. Eades, Nature 182, 1659 (1958); 183, 1802 (1959); I.J. Lowe, Phys. Rev. Lett. 2, 285 (1959).

[2] C. Huguenard, F. Taulelle, B. Knott and Z. Gan, J. Magn. Reson. 156, 131 (2002).

[3] T. Mizuno, T. Nemoto, M. Tansho, T. Shimizu. H. Ishii and K. Takegoshi, J. Am. Chem. Soc. 128, 9683 (2006).

[4] S.W. Sparks and P.D. Ellis, J. Am. Chem. Soc. 108, 3215 (1986).

[5] T. Mizuno and K. Takegoshi, JP Pat. No. 5445754 (B2) (2009); US Pat. No. 8547099 (B2) (2010); EP Pat. No. 2306215 (A1) (2010).

[6] K. Takeda, Rev. Sci. Instrum., 78, 033103 (2007); K. Takeda, Annual reports on NMR Spectroscopy, Vol. 74 Chap. 7.

[7] S.C. Shekar, D.K. Lee, and A. Ramamoothy, J. Magn. Reson. 157, 223-224 (2002).

[8] J.S. Frye and G.E. Maciel, J. Magn. Reson. 48, 125 (1982).

[9] S. Mamone, A. Dorsch, O.G. Johannessen, M.V. Naik, P.K. Madhu and M.H. Levitt, J. Magn. Reson. 190, 135 (2008).

[10] E. Mihaliuk and T. Gullion, J. Magn. Reson. 223, 46 (2012).

Figure Captions

Fig. 1

Schematic of the X_0 shim coil (a) and the effective magnetic field produced by the coil (b). The spinner axis of the sample lies in the xz plane. $2a, 2l$ and 2α are the coil diameter, the height and the gap angle between the two opposed arcs, respectively. The angle ε in (b) represents misalignment of the X_0 shim coil from the x axis.

Fig. 2

Schematic of a coordinate d along the spinner axis (a) and the calculated magnetic field B_x at $d = 0$ mm (b) and B_z at $d = 2.3$ mm (c). It was assumed that $I = 1$ [A] flows through the one-turn surface coil with the diameter of $2a = 66.4$ mm and the gap angle of $2\alpha = 30°$. The height $2l$ was used as a variable. The vertical dashed lines are drawn at $l = \sqrt{2}a \simeq 46$ mm (left) and $l = 69$ mm (right) for eye guidance.

Fig. 3

Schematics of a coil section wound by round wire (a) and rectangular wire (b). Note that, in (a) and (b), the cross-section areas of each wire are almost equal. (c) illustrates one of the pair of a flatwise-winding coil wound with the rectangular wire and a part of its outermost turn.

Fig. 4

Sketch of an X_0 shim coil on a mounting retainer attached to a MAS NMR probe in a main magnet with a room-shim unit.

Fig. 5

Calculated B_x (a) and B_z (b) along the spinner axis d for the 50-turn X_0 shim coil. The details of the coil dimensions are given in text.

Fig. 6

Schematic of pulsed current I synchronized to a single-pulse sequence. A rectangle followed by FID (top) represents a 90° pulse. To stabilize current I and the tilt-angle of the X_0 shim coil $\varepsilon(I)$, rf pulsing starts 400 ms after I reaches the target value. After acquisition of FID, the current is linearly decreased to the opposite current $-I$ in 200 ms and stays there for 100 ms to reduce accumulation of tilting of the X_0 shim coil due to the Lorentz force. The current is finally returned linearly back to 0 A in 300 ms.

Fig. 7

Observed full width at half maximum (FWHM) of ^{1}H MAS spectra of 5 mM $CuSO_4$ solution at various current I; the filled and open circles indicate with and without the correction of the xz-term of the room shim (C_{xz}), respectively.

Fig. 8

Observed dependence of the ^{13}C CPMAS spectra of adamantane on current I for the X_0 shim coil. The spectra are plotted on the same amplitude scale, and they can be directly compared.

Fig. 9

Dependence of the coil-tilt angle ($\varepsilon(I)$) of the X_0 shim coil on current I. $\varepsilon(I)$ was calculated from the observed shifts in Fig. 8 using Eq. (16). The straight line through the data points is the least-squares fitted one (Eq. (19)). The

dashed lines at $I = 0$ A and $\varepsilon(I = 0)$ are for eye guidance.

Fig. 10

Long-time stability of the coil-tilt angle ε at $I = \pm 5$ A with (the open circles) and without (the crosses) the $-I$ procedure in the pulse sequence (Fig. 6). In each series, the first ε value is set to be 0.

Fig. 11

Dependence of ^{2}H MAS spectra of dimedone-2,3-d_2 (inset) on current I.

Fig. 12

Dependence of the sum of the sideband peak-intensities of the ^{2}H MAS spectra of dimedone-2,3-d_2 on current I. The peak intensities for those within the $\pm$9th sidebands were added.

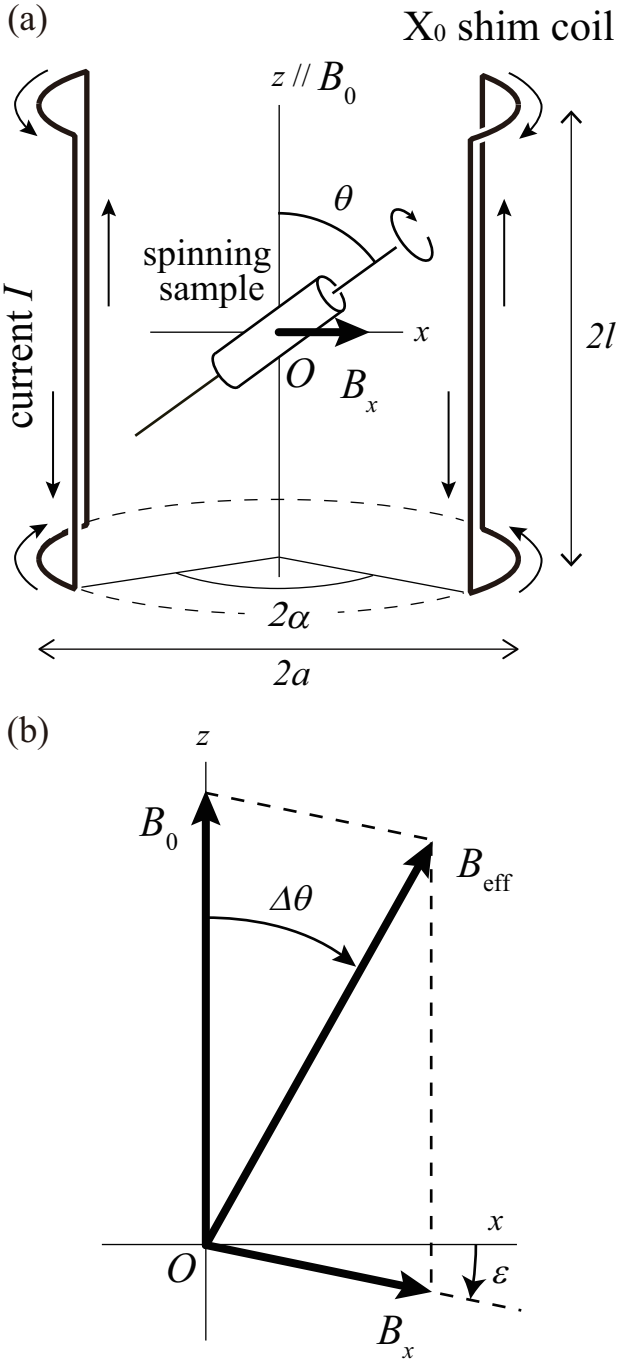
(a)
X0 shim coil
z // B0
θ
spinning
sample
x
O
Bx
current I
2l
2α
2a
(b)
z
B0
Beff
Δθ
x
O
ε
Bx

Fig. 1

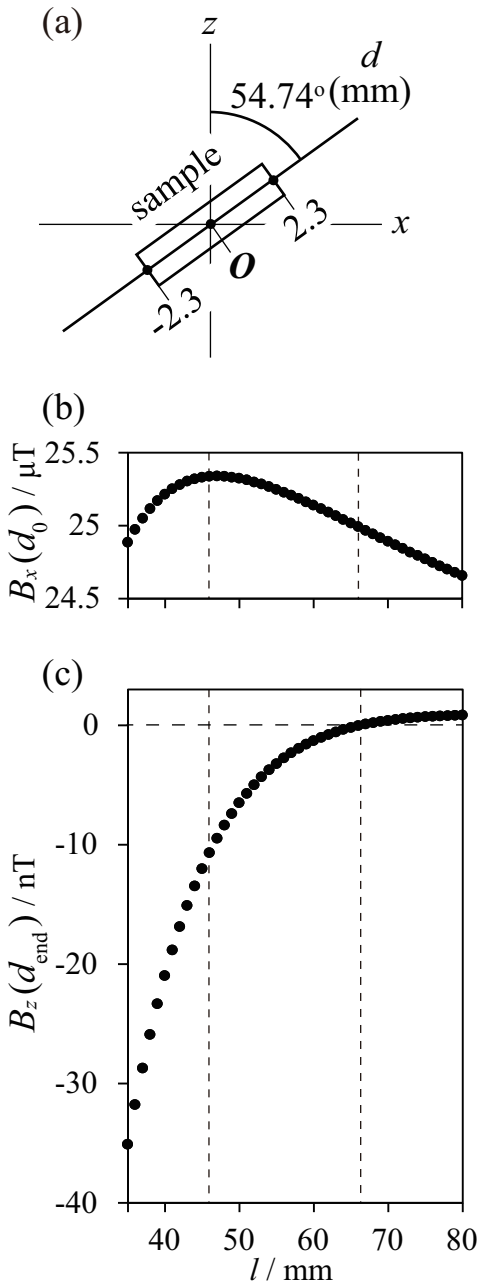
(a)
z
d
54.74°(mm)
sample
2.3
x
O
-2.3
(b)
$B_x(d_0)$ / μT
25.5
25
24.5
(c)
0
-10
-20
-30
-40
$B_z(d_{end})$ / nT
40
50
60
70
80
l / mm

Fig. 2

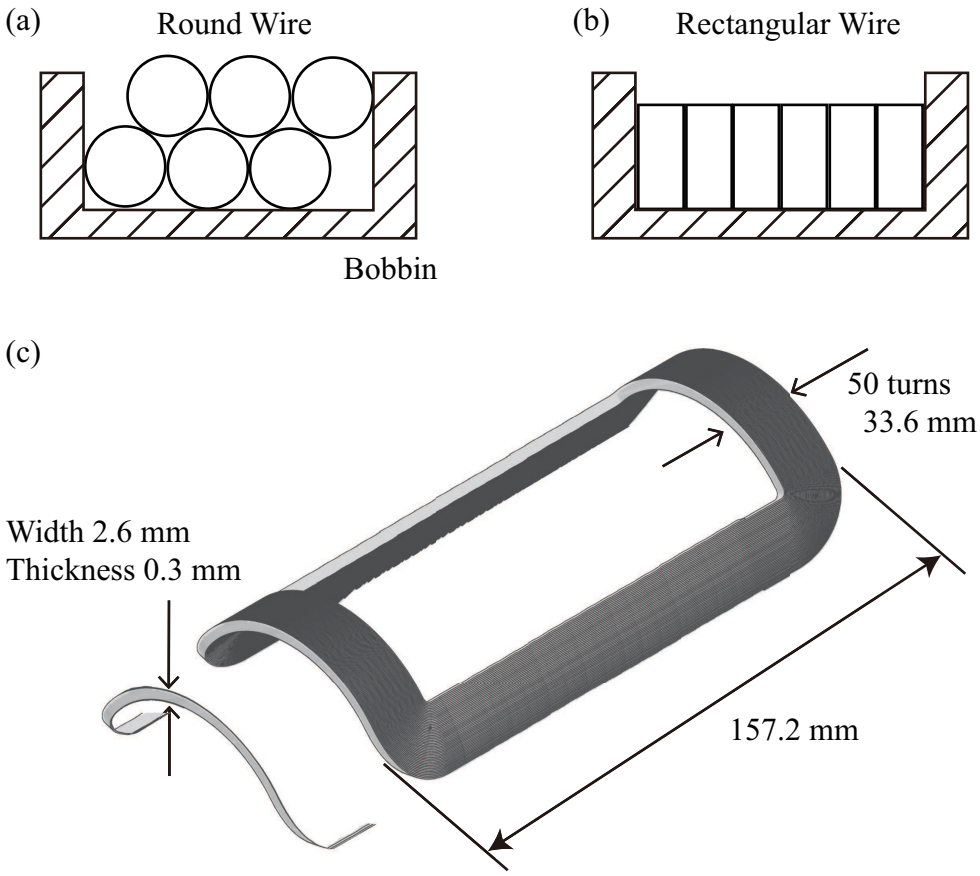
(a)
Round Wire
Bobbin
(b)
Rectangular Wire
(c)
50 turns
33.6 mm
Width 2.6 mm
Thickness 0.3 mm
157.2 mm

Fig. 3

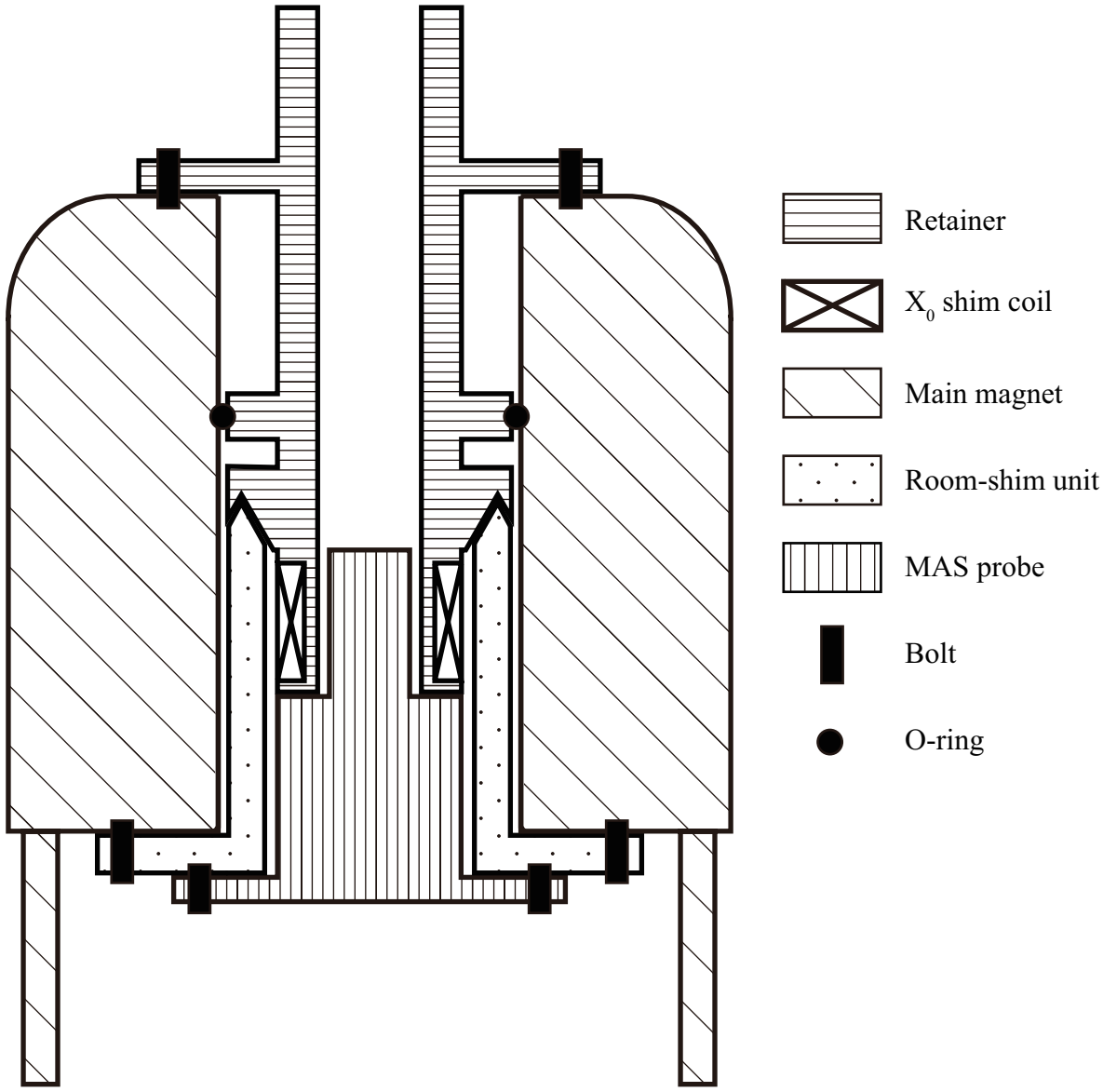
Retainer
X_0 shim coil
Main magnet
Room-shim unit
MAS probe
Bolt
O-ring

Fig. 4

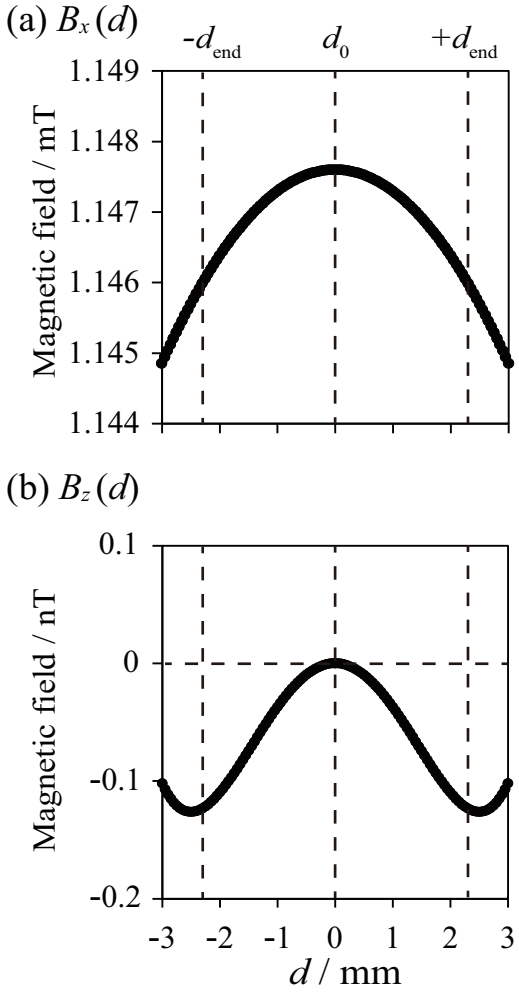
(a) $B_x(d)$
$-d_{end}$
d_0
$+d_{end}$
1.149
1.148
1.147
1.146
1.145
1.144
Magnetic field / mT
(b) $B_z(d)$
0.1
0
-0.1
-0.2
Magnetic field / nT
-3
-2
-1
0
1
2
3
d / mm

Fig. 5

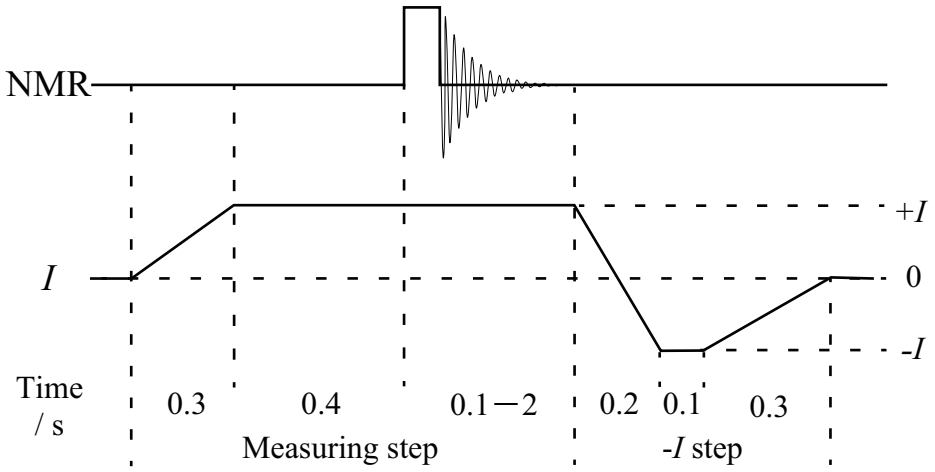

Fig. 6

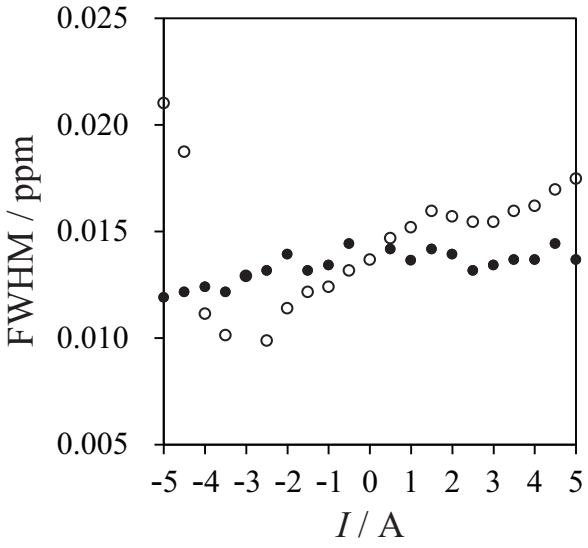

Fig. 7

Matsunaga et al.

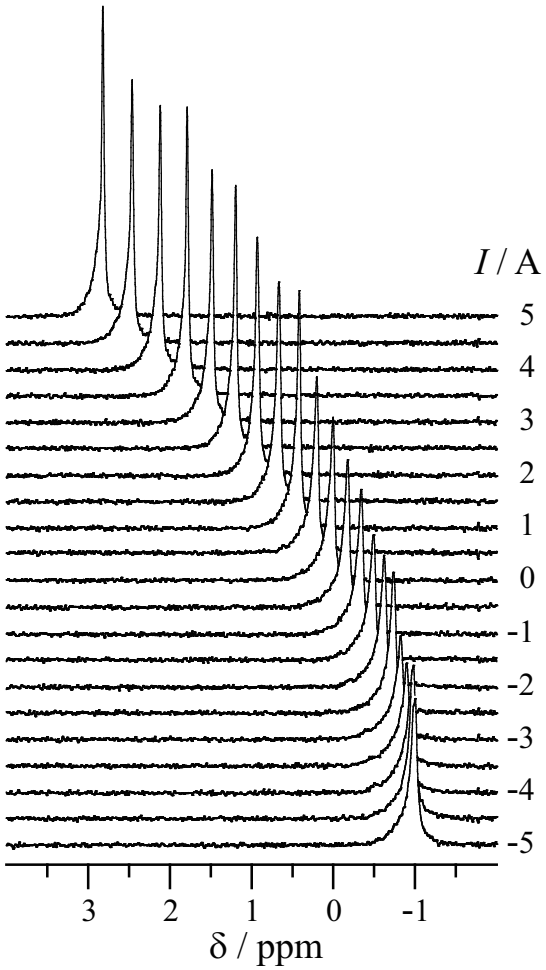

Fig. 8

Matsunaga et al.

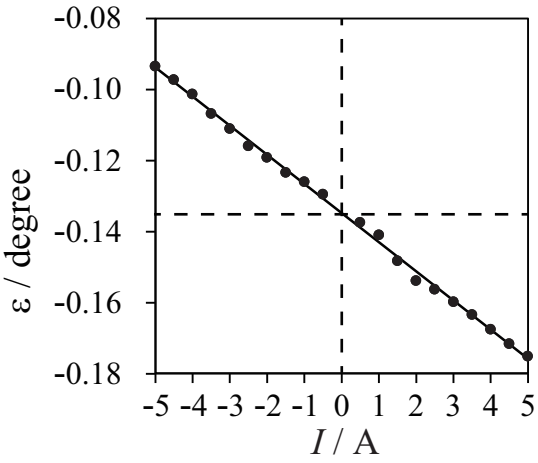

Fig. 9

Matsunaga et al.

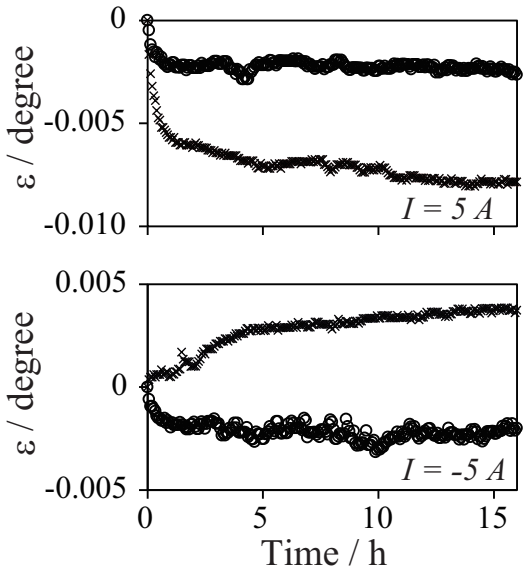

Fig. 10

Matsunaga et al.

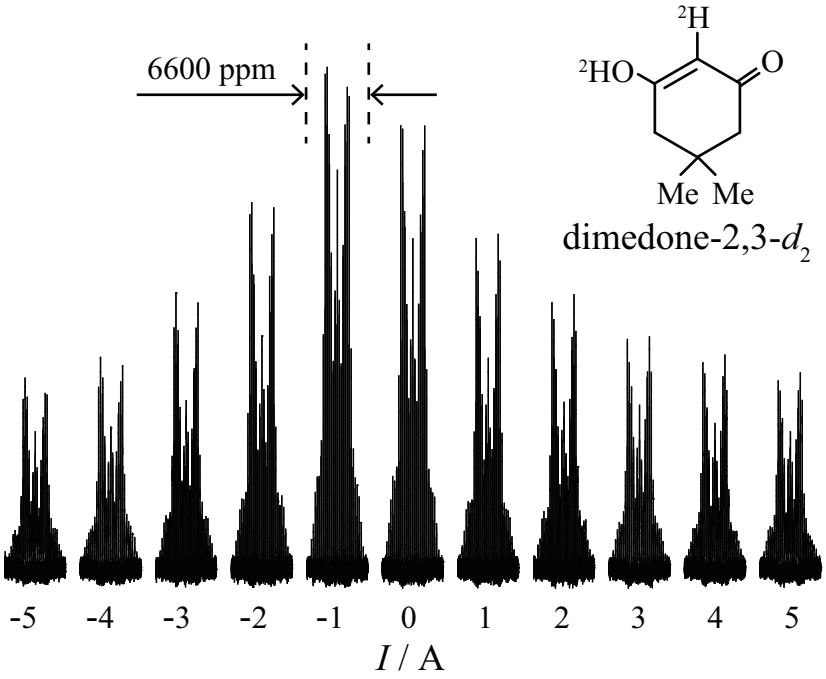

Fig. 11

Matsunaga et al.

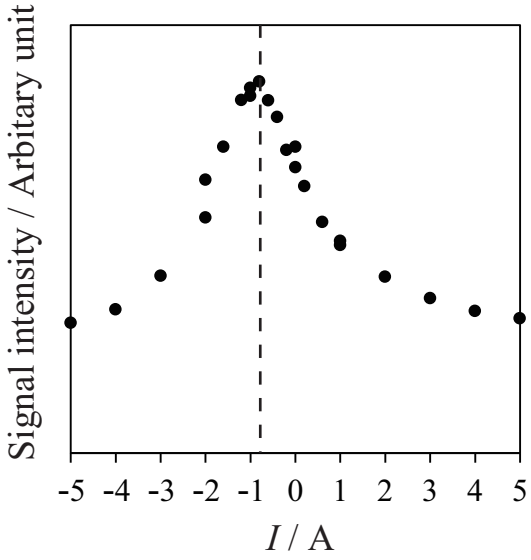

Fig. 12

Matsunaga et al.

An X_0 shim coil for precise magic-angle adjustment

Tatsuya Matsunaga [a], Takashi Mizuno [b], K. Takegoshi [a,*]

[a] *Division of Chemistry, Graduate School of Science, Kyoto University, 606-8502 Kyoto, Japan*

[b] *JEOL RESONANCE Inc., 196-8558 Akishima, Tokyo, Japan*

Supplementary materials

Contents

* corresponding author; takeyan@kuchem.kyoto-u.ac.jp

Preprint submitted to Elsevier Science

S1. Explicit integral paths for B^A

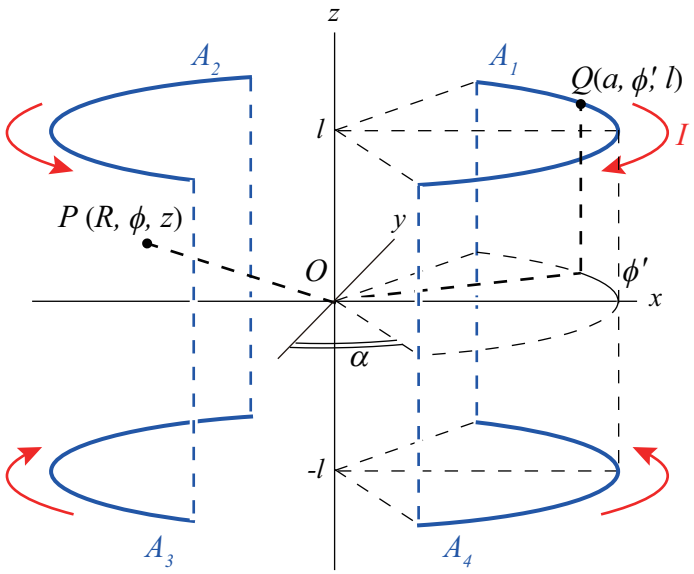

Fig. S1

Schematic of the arc parts of the X_0 shim coil (blue solid line).

Fig. S1 illustrates the direction of current I in the arc parts of the X_0 shim coil for $B_x^A > 0$ (red arrow). The arc parts is separated into the upper two parts (A_1 and A_2) and lower two (A_3 and A_4), respectively, and the corresponding integral paths are given as follows,

$$A_1 = \left\{ Q(a, \phi', l) \quad : \phi' = \left[\frac{\pi}{2} - \alpha \to -\frac{\pi}{2} + \alpha \right] \right\}, \tag{S1-1}$$

$$A_2 = \left\{ Q(a, \phi', l) \quad : \phi' = \left[\frac{\pi}{2} + \alpha \to \frac{3\pi}{2} - \alpha \right] \right\}, \tag{S1-2}$$

$$A_3 = \left\{ Q(a, \phi', -l) : \phi' = \left[-\frac{\pi}{2} + \alpha \to \frac{\pi}{2} - \alpha \right] \right\}, \tag{S1-3}$$

and

$$A_4 = \left\{ Q(a, \phi', -l) : \phi' = \left[\frac{3\pi}{2} - \alpha \to \frac{\pi}{2} + \alpha \right] \right\}. \tag{S1-4}$$

The integral paths in Eqs. (6) and (7) in the text are given by $C_{\rm high} = A_1 + A_2$ and $C_{\rm low} = A_3 + A_4$, respectively.

S2. Explicit integral paths for $\boldsymbol{B^L}$

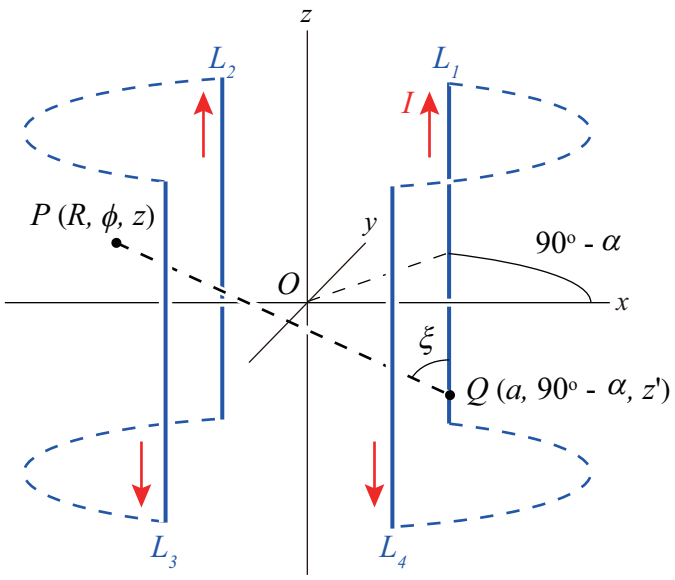

Fig. S2

Schematic of the line parts of the X_0 shim coil (bule solid line).

Fig. S2 illustrates the direction of current I in the line parts of the X_0 shim coil for $B_x^L > 0$ (red arrow). The corresponding integral paths are given as follows,

$$L_1 = \left\{ Q(a, \phi_1', z') : \phi_1' = \frac{\pi}{2} - \alpha,\ z' = [-l \to l] \right\}, \tag{S2-1}$$

$$L_2 = \left\{ Q(a, \phi_2', z') : \phi_2' = \frac{\pi}{2} + \alpha,\ z' = [-l \to l] \right\}, \tag{S2-2}$$

$$L_3 = \left\{ Q(a, \phi_3', z') : \phi_3' = -\frac{\pi}{2} - \alpha,\ z' = [l \to -l] \right\}, \tag{S2-3}$$

and

$$L_4 = \left\{ Q(a, \phi_4', z') : \phi_4' = -\frac{\pi}{2} + \alpha,\, z' = [l \to -l] \right\}. \tag{S2-4}$$

With these, we can analytically evaluate the integral of Eq. (8), and the result is

$$\begin{aligned} B_x^{L_i}(\boldsymbol{P}) = \frac{\mu_0 I}{4\pi} & \frac{a\sin\phi_i' - R\sin\phi}{a^2 + R^2 - 2aR\cos\phi_i'} \\ & \times \left\{ \frac{l - z}{\sqrt{a^2 + R^2 - 2aR\cos(\phi_i' - \phi) + (l - z)^2}} \right. \\ & \left. + \frac{l + z}{\sqrt{a^2 + R^2 - 2aR\cos(\phi_i' - \phi) + (l + z)^2}} \right\}. \end{aligned} \tag{S2-5}$$

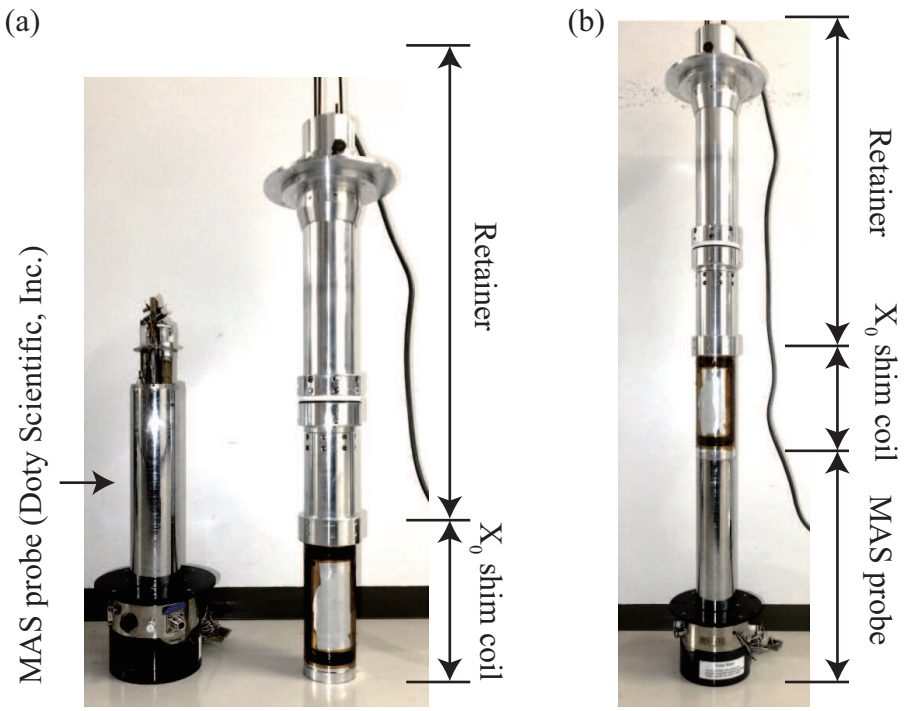

Fig. S3

A photograph of a MAS probe (Doty Science, Inc.) without its original cap and the X_0 shim coil on the retainer (a), which is used as a cap of the MAS probe (b).

S4. C_{xz} correction

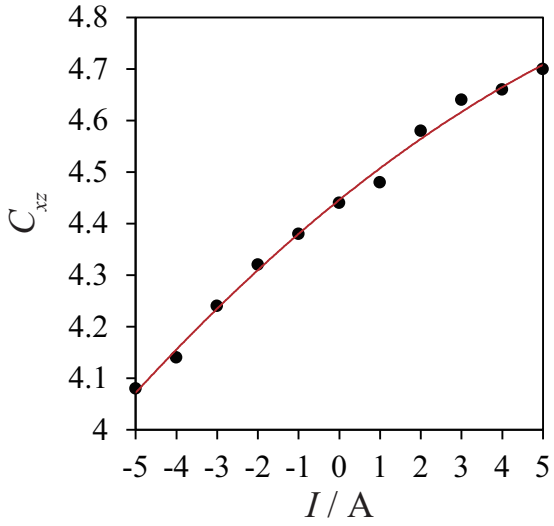

Fig. S4

Dependence of the optimum xz-term value C_{xz} of our room-shim unit on current I for the X_0 shim coil. C_{xz} was obtained by observing ^{1}H MAS NMR spectra of H_2O doped $CuSO_4$ (the measuring condition is same as that shown in the text).

Fig. S4 shows that the magnetic-field homogeneity around the sample was disturbed by the redundant magnetic field produced by the X_0 shim coil. The I-dependent C_{xz} values can be least-squares fitted to a quadric curve (red line) described as

$$C_{xz} = -0.0022I^2 + 0.0636I + 4.44. \qquad \text{(S4-1)}$$

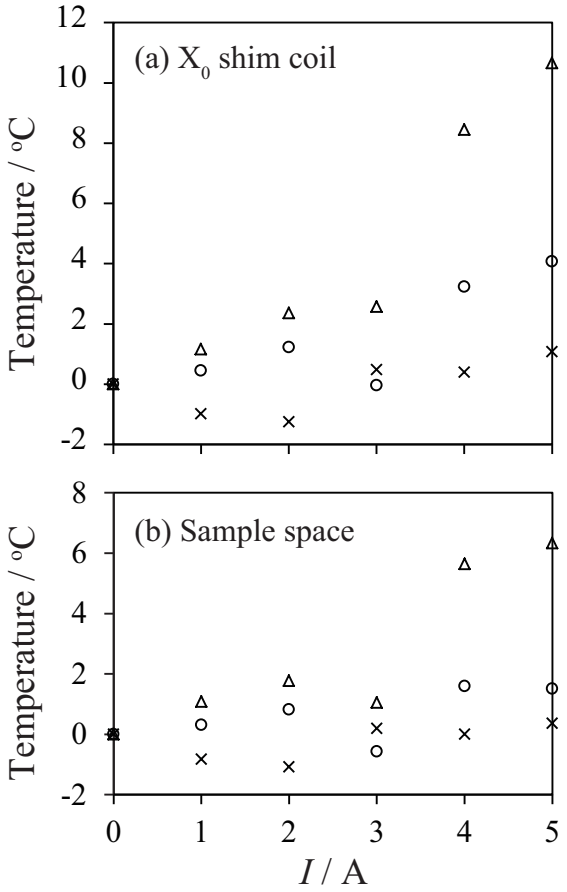

Fig. S5

I-dependent temperature due to the Joule heat at the X_0-shim-coil surface (a) and at the sample space (b). In both figures, the triangles, circles, and the crosses represent temperatures obtained without air flow, with the cooling air flowing from the bottom of the probe, and with both of the cooling air and the turning off of current I during relaxation time (Fig. 6), respectively. The temperatures were measured by chromel-copper thermocouples. The pulse interval was 5 s (1 s acquisition time and 4 s relaxation time).

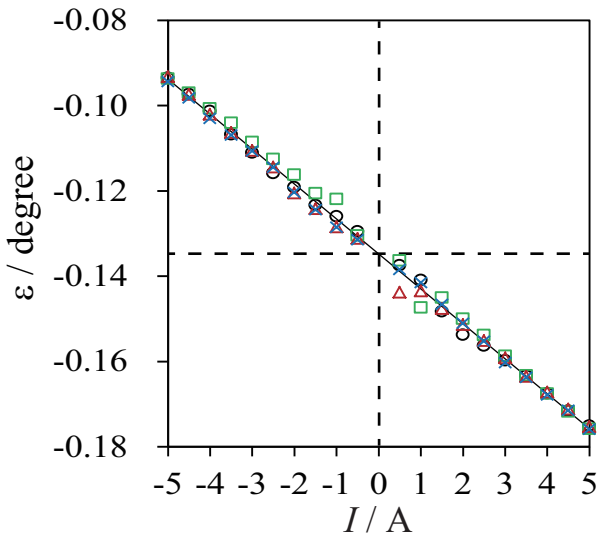

Fig. S6

Dependence of the tilting angle of the X_0 shim coil on current I. I was (1) increased from -5 A to 5 A (black circles), (2) decreased from 5 A to -5 A (green squares), (3) started from 0 A to 5 A, and jumped back to 0 A followed by decreasing to -5 A (red triangle), and (4) changed rather randomly as 0, 5, -0.5, 4.5, $\cdots$ A (blue crosses). The solid line through the data points is the least-squares fitted one described in the text (Eq. (19)).